Geophysical Prospecting

EAGE EUROPEAN ASSOCIATION OF GEOSCIENTISTS & ENGINEERS

Geophysical Prospecting, 2013, **61**, 187–199 doi: 10.1111/j.1365-2478.2012.01037.x

A numerical comparison of time and frequency-domain marine electromagnetic methods for hydrocarbon exploration in shallow water

Dylan Connell* and Kerry Key

Scripps Institution of Oceanography, La Jolla, CA, USA.

Received June 2011, revision accepted September 2011

ABSTRACT

In shallow water the frequency domain controlled source electromagnetic method is subject to airwave saturation that strongly limits the sensitivity to resistive hydrocarbon targets at depth. It has been suggested that time-domain CSEM may offer an improved sensitivity and resolution of these deep targets in the presence of the airwave. In order to examine and test these claims, this work presents a side-by-side investigation of both methods with a main focus on practical considerations, and how these effect the resolution of a hydrocarbon reservoir. Synthetic noisy data for both time-domain and frequency domain methods are simulated using a realistic frequency dependent noise model and frequency dependent scaling for representative source waveforms. The synthetic data studied here include the frequency domain response from a compact broadband waveform, the time-domain step-response from a low-frequency square wave and the time-domain impulse response obtained from pseudo-random binary sequences. These data are used in a systematic resolution study of each method as a function of water-depth, relative noise and stacking length. The results indicate that the broadband frequency domain data have the best resolution for a given stacking time, whereas the time-domain data require prohibitively longer stacking times to achieve similar resolution.

Key words: Marine CSEM, Marine Electromagnetics, Resistivity, Resolution, Uncertainty.

1 INTRODUCTION

The frequency domain marine controlled source electromagnetic (CSEM) method is now routinely used to map resistive hydrocarbons beneath the sea-bed (Ellingsrud et al. 2002; Constable 2010; Key 2011). The method was originally invented to determine the high resistivity of the lithosphere in the deep ocean (Cox 1980; Young and Cox 1981). Here the thick conductive ocean greatly attenuates the high frequencies of the naturally occurring magnetotelluric (MT) signal, so that active sources are required for imaging electrical structure at shallow crustal depths. Although the MT signal is stronger at shallower water depths, the currents it induces flow predominantly horizontal and therefore MT is sensitive only to relatively thick resistors such as salt structures (e.g., Hoversten, Morrison and Constable 1998; Key, Constable and Weiss 2006); conversely, the complex geometry of the CSEM fields emitted by an electric-dipole transmitter can offer strong sensitivity to the thin resistive layers formed by hydrocarbon reservoirs.

Despite this advantage, CSEM surveys in shallow water (<500 m) are subject to saturation by an airwave (e.g., Constable and Weiss 2006). This airwave contamination is the result of transmitted energy diffusing up through the shallow ocean, through the atmosphere and then down to seafloor EM receivers. In the non-conducting atmosphere there is no inductive attenuation of energy, whereas energy travelling through

*Now at Newmont Mining Corporation, Denver, CO, USA. E-mail: connell.dylan@gmail.com, kkey@ucsd.edu

the conductive seawater and seafloor experiences strong inductive attenuation. Because energy travelling in the atmosphere only decays by geometric spreading, it will ultimately dominate over the energy travelling through the seafloor and seawater, leading to the airwave dominating seafloor EM responses at long source-receiver offsets (e.g., Key 2011). The offsets at which the airwave saturation begins depends on the ocean depth, occurring within a few kilometres offset in 100 m water but not until 15 km or more offset in 1 km water. Since long offsets (several kilometres) are typically required to map deep resistive reservoirs (1-2 km below the sea-bed), airwave saturation in a shallow ocean can severely reduce the CSEM sensitivity to hydrocarbon reservoirs.

Amundsen et al. (2006) proposed to remove the airwave by a decomposition of the recorded EM fields into up and down-going components. However, the size of the airwave has been noted to be strongly coupled to the seabed resistivity and ocean thickness (Chave and Cox 1982; Andreis and MacGregor 2008; Orange, Key and Constable 2009); consequently, such a decomposition depends on a priori knowledge of the seabed conductivity, making its implementation potentially troublesome in regions of unknown or highly variable seafloor resistivity. The vertical electric field has been suggested to be beneficial for shallow water surveys since it is not masked by the airwave (Um and Alumbaugh 2007).

It has also been proposed that time-domain data are superior to frequency domain data in these shallow environments because of differences in the diffusion times of the airwave and energy traveling through the seafloor and reservoir. In shallow water the airwave arrival occurs at early times and the reservoir response at late times, allowing for their separation (Weiss 2007; Li and Constable 2010). Conversely, Andreis and MacGregor (2008) suggested using the standard frequency domain method but with a broad-spectrum source and a subsequent mode decomposition of the fields to accentuate the TM component that is less sensitive to shallow water effects.

Although reservoir sensitivity is diminished in shallow water, there have been successful CSEM surveys in the North Sea reported in the literature. MacGregor et al. (2006) used frequency domain imaging to map the Nuggets-1 gas field in 115 m water depths. Mittet (2008) demonstrated the application of the up-down decomposition separation to data from the Troll Field in 300 m water. Ziolkowski et al. (2010) documented the successful application of time-domain EM at the North Sea Harding field in 110 m water depths.

Despite the ongoing discussion of the relative merits of frequency and time-domain methods and the collection of field data sets, little has been done to quantitively compare their resolving capabilities in shallow water. The Fourier transform shows that the time and frequency domain methods are fundamentally related; however, the practical implementation details of each method may have a major impact on their respective resolving capabilities. The purpose of this work is to conduct a side-by-side investigation of both methods with a main focus on practical considerations and how these effect the resolution of a hydrocarbon reservoir. We begin by examining the sensitivity of frequency domain and time-domain methods to a thin resistive layer beneath the seafloor in shallow water. A realistic noise model is then introduced for the creation of synthetic noisy data. These data are then used in a systematic resolution study of each method as a function of water-depth, relative noise and stacking length.

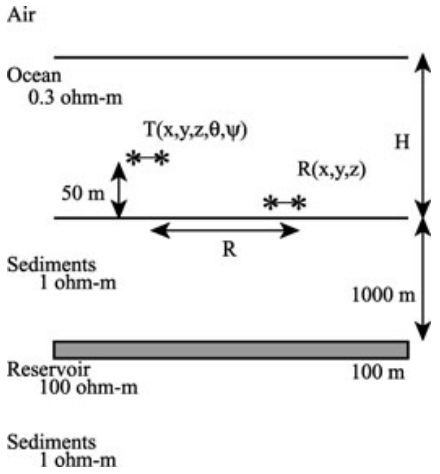

Figure 1. The 1D reservoir model, consisting of a highly resistive air layer above an ocean (0.3 Ωm) with depth *H* and underlying porous sediments (1 Ωm). A 100 m thick, 100 Ωm resistive layer representing a hydrocarbon reservoir lies 1000 m below the seafloor.

2 SENSITIVITY TO A THIN-RESISTOR

We begin our comparison of time and frequency domain EM methods by examining their respective sensitivities for a standard exploration model known as the canonical 1D reservoir. This model is composed of a highly resistive air layer above a 0.3 Ωm ocean and conductive 1 Ωm porous sediments. A 100 m thick, 100 Ωm resistive layer representing a hydrocarbon reservoir is positioned 1000 m beneath the seafloor, as shown in Fig. 1. For the shallow water problem considered here, we use a nominal ocean thickness of 100 m, except where noted otherwise. Although there are many possible source and receiver geometries as well as recorded field components, for

simplicity we only consider the in-line horizontal electric field since it has been shown to have the best resolution for a buried resistor (Key 2009).

Frequency domain CSEM responses were computed using the open-source 1D modelling code *Dipole1D* (Key 2009). Time-domain impulse and step-on responses were then generated by Fourier transformation of the frequency domain responses using the digital filter method (e.g., Anderson 1982; Newman, Hohmann and Anderson 1986). Due to the causality of the problem, the Fourier transform can be evaluated efficiently using either a sine or cosine transform (see Appendix A). Here we used the sine transformation, which was implemented using a 101 point digital filter that was optimized for marine CSEM using the methods discussed in Kong (2007) and Guptasarma and Singh (1997). Further details are provided in Connell (2011).

CSEM responses were computed for receivers spaced from 1 - 20 km offset from the transmitter and frequencies of 0.01-100 Hz for the frequency domain responses and times of 0.01 -100 s for the time-domain impulse and step-on responses. Responses were computed for both the canonical model and a reference model of the background sediments without the resistive reservoir.

Figure 2 shows the resulting CSEM anomalies generated by taking the ratio of the responses from these two models. The frequency domain anomaly is large at frequencies less than about 1 Hz and ranges larger than a few kilometres. A similar frequency domain sensitivity calculation for deeper water (1000 m) given in Constable and Weiss (2006) shows a maximum ratio that is up to three orders of magnitude larger and centred around the higher frequency of 10 Hz. Here the largest anomaly ratio is less than 10 and is located at ranges and frequencies close to where the response amplitude decreases to values close to typical system noise levels.

As expected from the Fourier transform that links time-domain methods to frequency domain methods, the time-domain anomalies appear very similar to the frequency domain anomaly, where the biggest anomalies are again at large ranges but now at late times rather than low frequencies. Both time-domain responses have the strongest sensitivity to the reservoir after 1 s recording time. While the impulse response anomaly is greater than the step-on anomaly, the amplitude of the impulse response is generally less than that of the step-on response. The step-on anomaly is similar in size when compared to the frequency domain anomaly. Noting that time and frequency can be viewed as inversely proportional, there is similarity in the frequency domain anomaly being largest at

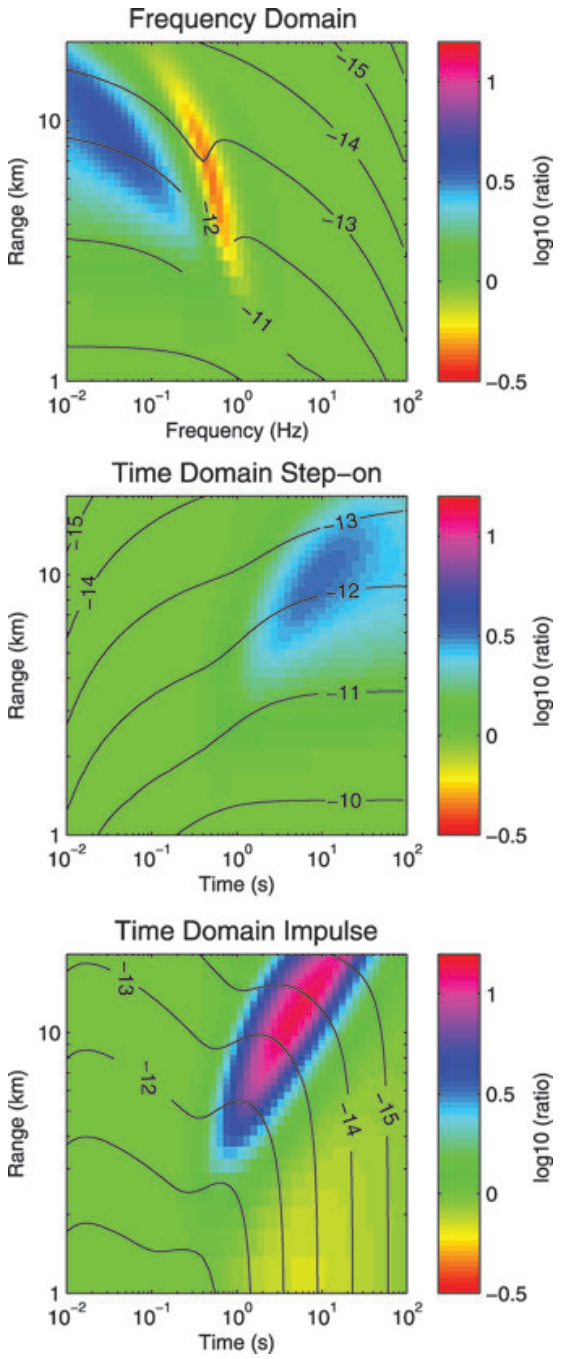

Figure 2. Sensitivity to the canonical reservoir model in 100 m water shown for frequency-domain, time-domain step-on, and time-domain impulse responses. CSEM anomalies were generated by taking the ratio of the responses from the canonical model and a similar model without the resistive reservoir. Black contours show $\log_{10}|E|$ in V/Am^2 for the canonical model.

frequencies less than 1 Hz while the time-domain anomaly is largest at times greater than 1 s.

From these simple anomaly studies we can conclude that the shallow water problem will be best tackled by long-offset recordings using low frequencies and late times. However, these high sensitivities are counteracted by a rapidly decreasing field amplitude that approaches or falls below the noise levels of typical acquisition equipment. Consequently, it will be important to consider the time and frequency domain characteristics of marine EM noise in the resolution tests presented below.

3 PRACTICAL CONSIDERATIONS

3.1 Source power

There are various transmitter waveforms available for frequency domain CSEM, as it has been the method of choice since the commercial development of marine EM exploration. Figure 3shows example amplitude spectra for a few representative waveforms. The simplest waveform is a periodic square wave in which the odd harmonics fall off in amplitude as $1/n$, where n is the fundamental period of the square wave. Since the square wave concentrates most of its power in the fundamental harmonic, the waveform period must be chosen carefully for a particular target, assuming sufficient knowledge of the host resistivity structure exists. This shortcoming of the square wave motivated the development of broadband waveforms that contain a wide suite of discrete frequency harmonics (e.g., Mittet and Schaug-Pettersen 2008; Myer, Constable and Key 2011). Figure 3 shows a selection of the largest harmonics of 'waveform D', the compact broadband waveform currently used by the marine EM group at the Scripps Institution of Oceanography (Myer et al. 2011). This waveform spreads much of the transmitted energy across the first decade of harmonics with its third and seventh harmonics being the largest. Like the square wave, only the odd harmonics are non-zero for waveform D. A major benefit of such broadband waveforms is that the higher frequencies can constrain shallow a structure while the lower frequencies constrain deeper features. The compactness of waveform D is advantageous for time-series processing using short time windows to reduce stacking bias and for generating an ensemble of samples for robust stacking (Myer et al. 2011).

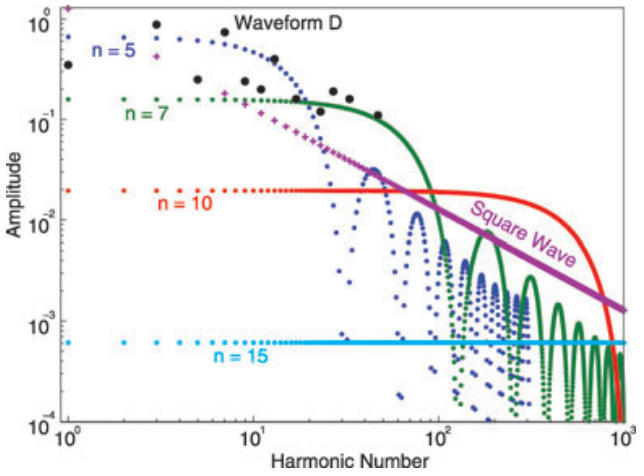

Figure 3. Comparison of the source amplitude spectra for a square wave (purple crosses), waveform D (large black dots), and PRBS sequences for n = 5 (blue dots), n = 7 (green dots), n = 10 (red dots), and n = 15 (cyan dots).

Time-domain step-on responses can be obtained by using a square waveform with a sufficiently long period such that the received electric field has approached its DC limit. From the sensitivity study shown in Fig. 2, this means a rectangular waveform with a period of at least several tens of seconds. Compared to the frequency domain use of the square wave, where the fundamental harmonic can be placed at a frequency with high target sensitivity, the time-domain use of the square waveform essentially moves the fundamental harmonic down to a much lower frequency associated with the DC limit. Therefore, the power will be significantly lower at the higher frequency harmonics where the data are sensitive to the target. As shown below, this lower source power must be compensated by significantly longer stacking in order to reduce the noise to levels comparable to typical frequency-domain waveforms.

The impulse response is more difficult to obtain. While in principle the impulse response can be computed by taking the numerical derivative of the recorded step-on responses, doing this with real data would be unwise since the differentiation can act to amplify noise. Instead, the impulse response can be obtained by transmitting pseudo-random binary sequences (PRBS) and then using deconvolution to obtain the impulse response (Duncan et al. 1980). The PRBS was recently used for the time-domain EM survey described in Ziolkowski et al. (2010). A PRBS (also known as a maximal length sequence) is created using a linear feedback shift register. For a shift register of length n, the PRBS will have length $2^n - 1$. A key property of the PRBS is that its autocorrelation approaches an impulse train with increasing n. Consequently, the impulse response can be recovered by deconvolution of the recorded receiver response and the measured PRBS waveform (e.g., Ziolkowski, Hobbs and Wright 2007).

Figure 3 shows the amplitude spectra for a few PRBS waveforms with varying n, illustrating that the PRBS contains both odd and even harmonics, unlike the symmetric square wave and waveform D. As the sequence length increases, the PRBS spectrum flattens to increasingly higher frequencies as it approaches the purely flat spectrum of an impulse. Therefore, as n increases, the deconvolution will better yield the impulse response. However, the increase in n comes with a strong decrease in the source amplitude. As we show later, this loss in source energy can be compensated by a concomitant increase in stacking length. For land based EM studies where much higher transmission frequencies are used, the additional time spent stacking is relatively negligible compared to other survey time-costs (e.g., Ziolkowski et al. 2007). Conversely, for the low frequencies required in the marine environment, the additional time needed to stack the PRBS signal could become prohibitive due to the bias introduced by a moving deep-towed transmitter. This led Ziolkowski et al. (2010) to use a transmitter that was parked on the seafloor during transmissions. A compromise would be to use a short PRBS with $n = 5$, which has a spectrum somewhat comparable to waveform D, although the PRBS drops off faster at high frequencies.

The frequency density of waveform D compared to the PRBS is worth considering. Waveform D only contains odd harmonics, whereas the PRBS has a factor of two increase in density since it has both odd and even harmonics, albeit at a lower amplitude. As Fig. 2 shows, CSEM responses vary smoothly in frequency, suggesting that there will probably be little advantage to the factor of two increase in frequency density for the PRBS. Another concern is the lower amplitude of the PRBS source, which results in a lower signal-to-noise ratio in the recorded data unless an accompanying increase in stacking is used to compensate for this loss.

3.2 A realistic noise model

In order to conduct a fair comparison of time and frequency domain methods, realistic noise characterizations in both domains must be included. We created a frequency domain noise model similar to that given in Constable and Weiss (2006) but with expanded terms in order to highlight the various sources of noise. The absolute electric field response noise E_a is characterized as:

$$E_a(f) = \frac{E_n(f)}{l_s I S(f)\sqrt{N}}, \tag{1}$$

where $E_n(f)$ is a frequency dependent electric field noise with units V/(m$\sqrt{\text{Hz}}$), l_s is the transmitter dipole length in metres, I is the source current intensity in amperes, $S(f)$ is the frequency dependent source spectrum described in the previous section and N is the window stack length in seconds. The product $l_s I$ is the source dipole moment, which here is taken to be 100 kAm (representative of a 500 A current on a 200 m dipole). The source current amplitude and phase are assumed to be stable enough that their contribution to the noise is negligible. This equation shows that the absolute noise can be reduced through a combination of a stronger dipole moment, a stronger source spectrum or a longer stacking length.

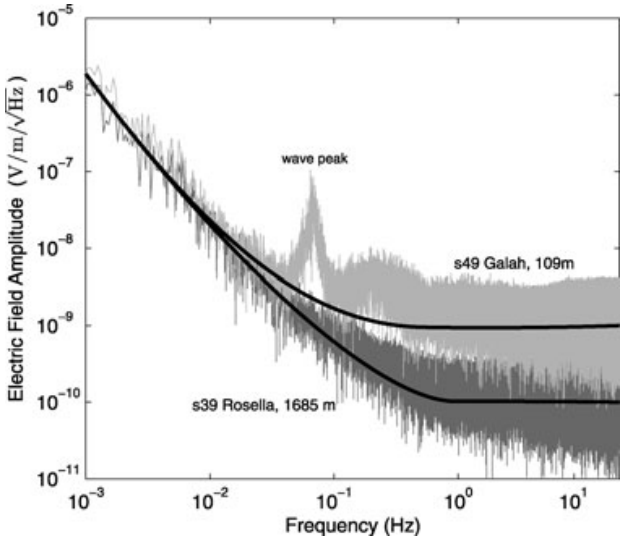

Figure 4. Electric field amplitude spectra for two seafloor receivers deployed on the continental shelf offshore the west coast of Nicaragua at water depths of 109 m (s49 Galah) and 1685 m (s39 Rosella). Spectra were computed from four hours of data starting on 2nd May 2010 04:00:00. The thick black lines show the noise models $E_n(f)$ used by this study for shallow and deep water.

The frequency dependent noise term $E_n(f)$ is independent of the CSEM transmitter system and can be expanded as

$$E_n(f) = E_i(f) + \frac{V_r(f)}{l_r}, \tag{2}$$

where $E_i(f)$ is the induced environmental noise from sources such as magnetotelluric signal, water currents and tides, and V_r is a frequency dependent voltage noise spectrum for the logging system electronics and the measurement electrodes. l_r is the length of the measurement electric dipole. This shows that the contribution from the voltage noise $V_r(f)$ can be reduced by using a longer receiving dipole l_r, whereas the contribution from the environmental noise $E_i(f)$ is independent of the measuring dipole length.

Figure 4 shows an example of $E_n(f)$ observed for two receivers deployed offshore Nicaragua as part of a 54 site

MT and CSEM survey of the Central American subduction zone (Key 2010). Both receivers used a modern version of the broadband instrumentation described in Constable et al. (1998). Site s49 was deployed on the shallow continental shelf in 109 m water and site s39 was deployed on the continental slope at 1685 m water depth. The amplitude spectra were computed from 4 hours of recordings using Welch's method (Percival and Walden 1993) and include the corrections for the frequency dependent system responses. The power spectra were first computed for each of the orthogonal horizontal electric channels and these were combined to yield the total horizontal electric power. This quantity was then plotted in the amplitude units required by equations (1) and (2).

At frequencies below about 0.05 Hz, both the shallow and deepwater receivers have a similar spectrum due to the spatially coherent MT signal. From the perspective of the CSEM data, the naturally occurring MT signal is viewed as noise. The spectra diverge at higher frequencies, with the shallow water site having significantly higher amplitude. For the deep water site, the attenuation of the magnetotelluric energy at frequencies above 1 Hz is severe (e.g., Key 2003), so the lower amplitude and relative flat spectrum at high frequencies are due to white noise from the logging electronics, which is represented in our noise model by the term $V_r(f)/I_r$. This noise is a characteristic of the system electric field noise-floor (Constable et al. 1998; Hoversten, Constable and Morrison 2000). The attenuation of the MT source field for the shallow site is negligible at frequencies below 10 Hz (Key 2003), so the higher amplitude here is due to a combination of the MT signal as well as noise associated with ocean waves and water currents. The prominent peak centred at 0.07 Hz for the shallow water site is the direct noise from the ocean waves. The wave height varied considerably during the entire 19 days deployment; the spectra computed for other time segments (not shown here) indicate that this wave peak is sometimes negligible while at other times can be up to five times larger. With the exception of the wave peak, the data shown here represent typical good quality data.

The black lines in Fig. 4 show the simplified noise models used here for shallow and deep water. Since the wave peak is variable in time and can impact each survey area to varying degrees, it was not included in the shallow water noise model. However, if wave noise is present, it may corrupt low-frequency CSEM measurements and therefore should be considered as a complicating factor when planning shallower water surveys.

In addition to the absolute electric field noise E_a, the effect of errors in the transmitter navigation, receiver orientations and locations and sensor calibrations must also be included. These are typically modelled as a multiplicative relative noise factor E_r, since they often scale with the measurement and can not be reduced by stacking. Combining the absolute and relative noise terms, the complete noisy data $\tilde{E}$ can then be represented by:

$$\tilde{E} = E_r E + E_a, \tag{3}$$

where E is the noise-free electric field. To generate the synthetic noisy data $\tilde{E}$ required in the studies below, we used random uniformly distributed phase noise along with the amplitude noise spectrum described above to create a frequency dependent Gaussian noise model for E_a. Random normally distributed relative noise was generated for E_r and then both terms were applied using equation (3) to generate the frequency domain noisy data $\tilde{E}$. The corresponding time-domain noise was created by the inverse Fourier transformation of $\tilde{E}$.

Figure 5 shows examples of the synthetic data generated for the time and frequency domain methods. Responses were computed using the absolute noise shown in Fig. 4, 1% relative noise and ten stacks. The frequency domain data consist of seven high power harmonics of waveform D with a 0.1 Hz fundamental harmonic. This corresponds to a 10 second waveform, with the ten stacks giving $N = 100$ s. The time-domain DC limit of the system is dependent on the offset of the receiver but is typically reached after about 10-30 s, suggesting that for this model a 30 s time-domain waveform is sufficient. For both time and frequency-domain methods, synthetic data with signal-to-noise ratios below one were not considered in the resolution studies that follow.

4 RESOLUTION OF A THIN RESISTOR

In order to characterize the resolution of each method to a thin resistor representing a hydrocarbon reservoir, we performed a perturbation analysis on the canonical reservoir model. The approach follows the method used by Key (2011) to examine the effects of multi-frequency data on resolution. Synthetic noisy data were created using the canonical model and a suite of perturbed models in which the reservoir resistivity and thickness were varied (but the depth to the resistive layer was kept the same). The responses were computed for eleven receivers placed along the seafloor at 1000 m intervals in in-line geometry, with the nearest receiver at 1000 m offset and the furthest at 11,000 m. The EM transmitter was located 50 m above the seafloor. This height is typical when towing a transmitter to avoid collisions with the ocean bottom. In the later model studies where the water depth is only 50 m, this

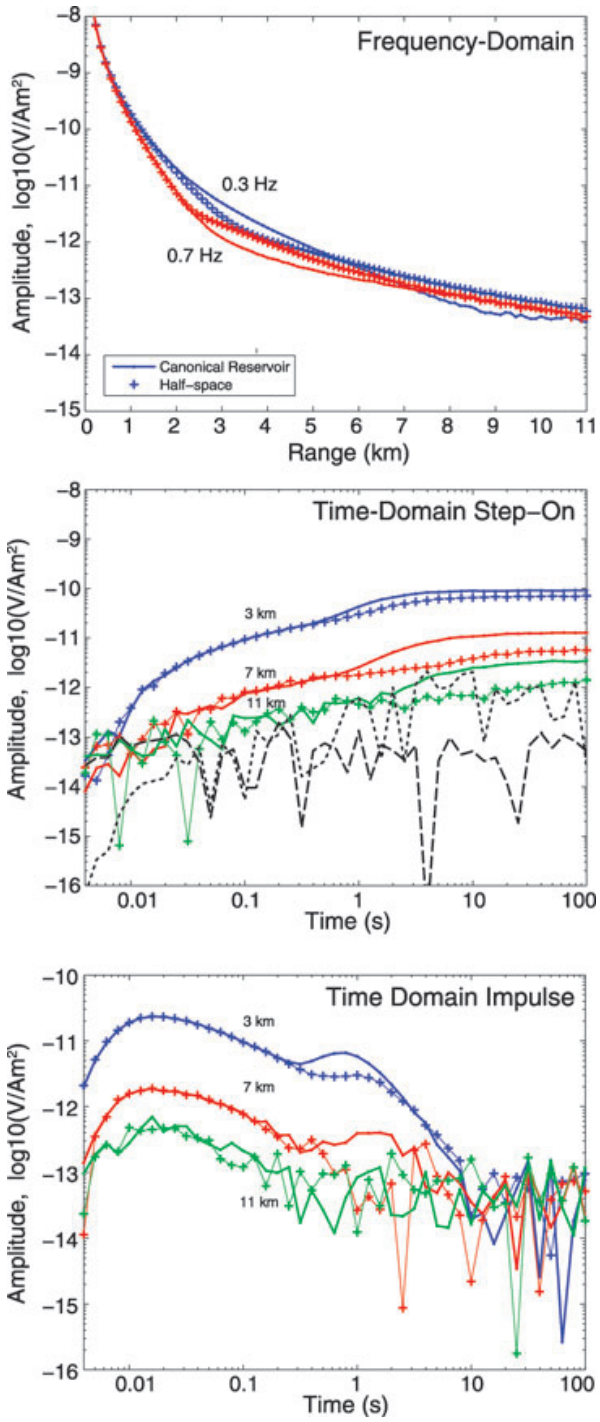

Figure 5. Example of noisy frequency-domain (top) and time-domain step-on (middle) and impulse (bottom) responses after applying the random electric field noise model. Only the third and seventh harmonics of waveform D are shown for the frequency-domain data. The step-on responses include the noise times series at 7 km offset for the absolute noise (long dashed black line) and the relative noise (short dashed black line).

implies a surface towed source. The perturbed models had the resistivity and thickness varied by up to a factor of 10 from the true canonical model. For each perturbed model, the root-mean-squared (RMS) misfit x_{rms} of its response d to the true unperturbed model response m was computed using

$$x_{rms} = \sqrt{\frac{1}{M}\sum_{i=1}^{M}\left(\frac{d_i - m_i}{\sigma_i}\right)^2}, \tag{4}$$

where M is the number of data and σ is the uncertainty from the noise model. For the frequency domain responses, the data d consists of real values of the amplitude and phase; for the time-domain responses d contains the real valued electric field. The RMS values were then plotted as a function of the perturbed thickness and resistivity of the reservoir. The ideal fit to the noisy data is $x_{rms} = 1$, where on average each datum is fit to the level of its uncertainty. The RMS misfit between time and frequency-domains is comparable through Parseval's theorem in which the L2 norm is preserved by the Fourier transform. This comparison via misfit mapping does not involve the use of any inversion algorithm and therefore will not be biased by particular choices of regularization and smoothing operators.

An example misfit study for 100 m water depth is shown in Fig. 6, which compares the resolution obtained by using a 60 s recording window for both waveform D and the step-on response. This allows for six 10 s stacks of the frequency domain data and two 30 s stacks of time-domain data. Both the frequency and time-domain studies have a low misfit region aligned along a band of nearly constant resistivity-thickness product. This illustrates that CSEM is predominantly sensitive to the resistivity-thickness product of a buried resistor, although bounds on the reservoir resistivity and thickness can be found in many cases. Here the frequency domain data are able to bound the maximum thickness of the resistor to a few hundred metres and similarly its minimum resistivity to about 50 Ωm. Clearly the lowest misfits occur in a small region around the true values. Conversely, the time-domain data contain low misfits across the entire range of resistivity-thickness products and therefore can not bound the minimum resistivity or the maximum thickness. The frequency domain data also have a significantly narrower low-misfit region, indicating their better resolution. This resolution disparity arises from the lower signal-to-noise ratio of the time-domain data due to the low power of the 30 s square waveform harmonics at higher frequencies.

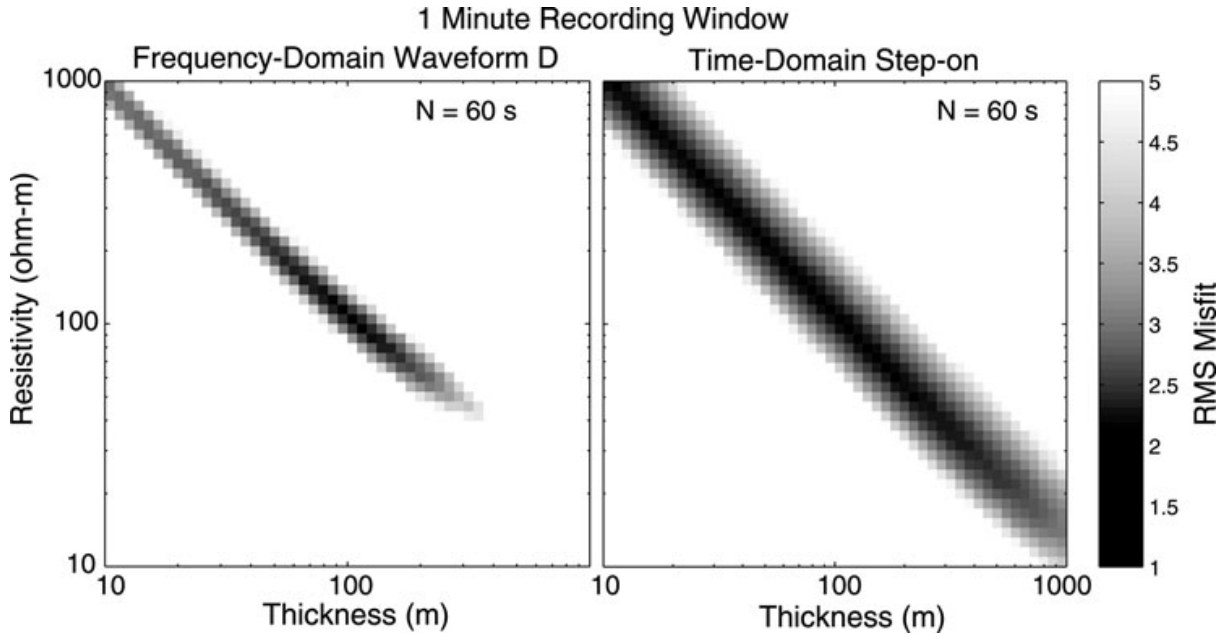

Figure 6. RMS misfit for perturbations to the canonical reservoir thickness and resistivity for both frequency-domain (left) and time-domain step-on responses (right) for $N = 60$ s acquisition, corresponding to six frequency-domain traces and two time-domain traces per datum. The water depth was 100 m. The true model contains a reservoir thickness of 100 m and resistivity 100 ohm-m.

4.1 Dependence on water depth

The resolution of a thin resistor is dependent on water depth. Airwave contamination and environmental noise in shallow water increase as water depth decreases. This is shown in Fig. 7, where the water depth in the 1D model is decreased from 1000 m to 50 m. The absolute noise was scaled for each water depth using an exponential scaling between the deep and shallow water noise curves shown in Fig. 4. The frequency domain data were stacked using 60 s of data, corresponding to six stacks of the 10 s traces. For the time-domain computations, 450 s of step-on data were used, which is equivalent to stacking fifteen 30 s traces. This was found to be long enough to compensate for the reduced source power of the 30 s time-domain waveform, as indicated by the similar appearance of the frequency and time-domain misfit surfaces shown in Fig. 7. At frequencies around 0.1-1 Hz the 30 s time-domain waveform has about 3–5 times less power than waveform D, which is then compensated with longer stacking for noise reduction through $\sqrt{N}$ in equation 1.

Figure 7 shows that as the water depth decreases, the range of resistivities and thicknesses that produce acceptable RMS misfits increases significantly. Therefore resolution is lost as the water shallows due to the airwave. The resolution to the thin resistive layer is much greater in deeper water, allowing for tighter bounds on the acceptable ranges of the resistivity and thickness. In the shallowest water depths (around 100 m) both methods appear to give similar results but again this was only obtained by significantly increasing the time-domain stacking length.

4.2 Dependence on stacking length

The signal-to-noise (SNR) ratio is perhaps one of the most influential factors controlling the resolution. In order to evaluate the benefits of stacking on the SNR, it is helpful to omit the relative noise and concentrate on only the absolute noise. Without relative noise there are very large SNRs (up to factors of 10^4) at receivers closest to the transmitter. This controls the misfit space and may be unrealistic, particularly at short ranges where positioning errors dominate the relative uncertainty.

The previous section considered time-domain responses to 30 s so that the full DC response was obtained. In this section the time-domain data used in the misfit computations are limited to 10 s time-offsets since very little additional resolving power is added by later times. Similarly, it is not useful to consider early time responses ($\leq$0.25 s). These responses contain very little geologic signal and are dominated by the airwave in shallow water, artificially driving the misfits down since their contribution is the same for all model perturbations without adding any additional geologic information.

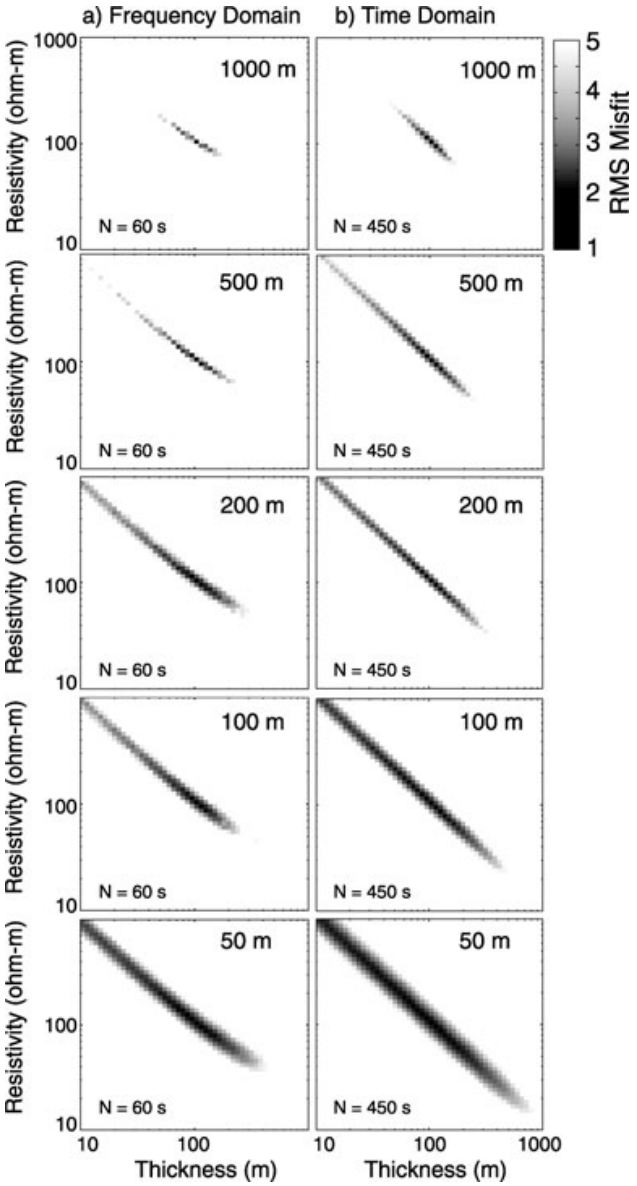

Figure 7. Misfit surfaces for both frequency-domain (waveform D) and time-domain (step-on) responses as a function of ocean depth. The water depth decreases from top to bottom from 1000 m to 50 m. The frequency-domain data used 6 stacks of 10 s traces ($N = 60$ s) while the time-domain data used 15 stacks of 30 s traces ($N = 450$ s).

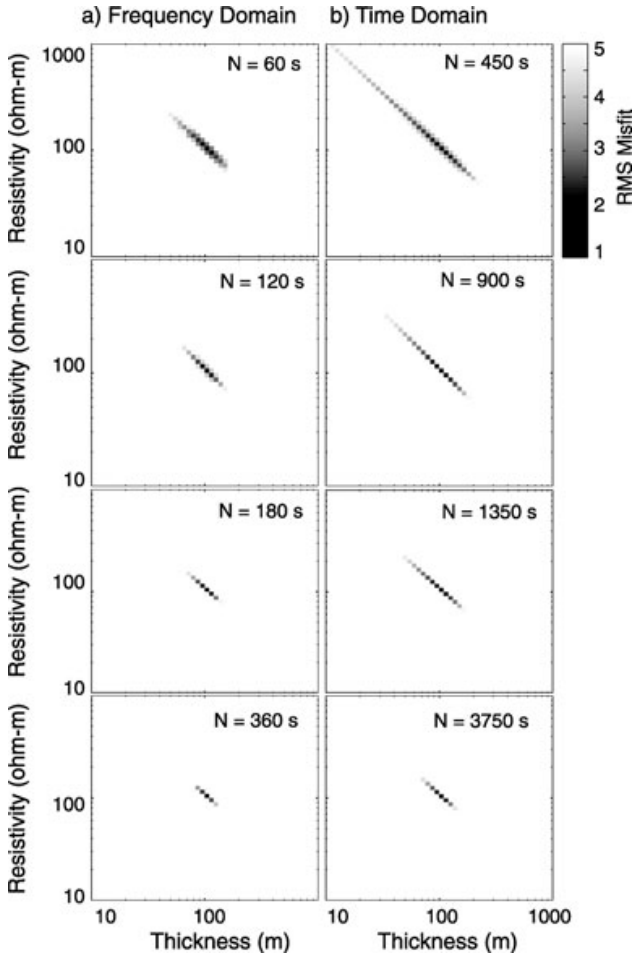

Figure 8. Misfit surfaces for the frequency-domain (waveform D) and time-domain (step-on) responses for various levels of stacking times (N) for the canonical model in 100 m of water. Relative errors due to errors in survey parameters were not included here, in order to isolate the effect stacking has on the absolute noise.

The benefits gained by various amounts of stacking are demonstrated in Fig. 8. As expected, stacking increases resolution and sensitivity in both domains. The time-domain data require large amounts of stacking to suppress the background noise. Roughly 1 hour of stacking is required in the time-domain in order to narrow down the area of acceptable misfit to what can be achieved using 180 s of stacking in the frequency domain. This factor of 20 difference in stacking times corresponds to a $\sqrt{N}$ factor of about 4.5, which again compensates for the lower source power of time-domain waveform at higher frequencies. This suggests not only that frequency domain methods are capable of having the same resolving power as time-domain methods but can do so with significant time savings over that required for time-domain methods, as the source power at frequencies sensitive to the reservoir is larger in the frequency domain. One could reduce the required amount of stacking by increasing the source dipole moment but increasing either the transmitter current or antenna length results in improvements for both domains. The smooth nature of the frequency responses also suggests that the dense frequency sampling by a step-on waveform is not required for high resolution and that the sparse frequency sampling in the

frequency domain is sufficient. Sparsely sampled frequency domain data will also be more independent than the densely spaced time-domain data.

Stacking time intervals are an important consideration in the marine environment and are directly related to ship survey time and cost. The recording window must be chosen to include as much target signal as possible without biasing the data. With a ship speed of 1-2 knots (0.5-1 m/s) and a data recording window of sixty seconds, the transmitter moves roughly 30-60 m (less than a source dipole length) per window in a frequency domain survey. Biasing of the data in this situation is not large (<1%) and can be corrected (e.g., Myer et al. 2011). Time-domain data will be severely biased from the long stacking windows shown here if the transmitter is towed at the same speeds as for frequency domain methods. Therefore, time-domain surveys commonly use a stationary transmitter that is subsequently moved between each source location. The stationary source and receiver setup requires additional time for transiting between acquisition locations. In order to reach the DC limit in time-domain data, the step-on response requires a longer recording window. If the target was deeper, say 2 km, this window would have to be even longer as the initial arrival time of the reservoir signal is on the order of a few seconds (Weiss 2007). These deep reservoirs also require large transmitter-receiver offsets, further hindering detectability since the signal-to-noise ratio decreases at large offsets.

4.3 Dependence on relative noise

This section examines the effect of relative noise E_r on resolution and expands the time-domain analysis to include PRBS data for an order n=10 sequence. The time-domain data were stacked using 3750 s of data (125 stacks of 30 s traces) while a 180 s window was used for the frequency domain data, due to these parameters exhibiting similar resolution in the previous section where no relative error was used. The PRBS data had synthetic noise added, were then processed using Wiener deconvolution, and finally were smoothed to recover the model impulse response. This processing may be considered a best case scenario due to the availability of the true power spectra of the target signal and noise. Misfits from waveform D, step-on, and PRBS data in 100 m water using various values of E_r are shown in Fig. 9.

All three methods exhibit better resolution capability as the relative error vanishes. For both 1% and 0.1% noise, the frequency-domain data have the best resolution while the PRBS is poorest (yet still reasonably good). When the relative noise is absent, the PRBS data offer the best resolution. For this case the PRBS does well due to the ideal performance of the deconvolution processing; however since relative errors are unavoidable with current acquisition technology, neglecting them or assuming they are vanishingly small is unrealistic.

Accuracy in parameters such as transmitter and receiver location has improved recently due to advancement in acoustic navigation technology but significant position uncertainties are still encountered. A typical value assigned to this uncertainty is 1%. The benefits created by increasing signal-to-noise ratios by stacking are then limited by this percentage. At short offsets where the responses decay very rapidly with range, the transmitter location uncertainty is one of the largest sources of error. This uncertainty can be significantly decreased in shallow water by using a surface towed array in which the source location can be tracked by GPS devices with a much higher precision than available for acoustic navigation of deep-towed transmitters. Shallow water modeling done by Li and Constable (2010) showed that there is no clear disadvantage to tows in which the transmitter, receivers, or both are located at the sea-surface rather than the sea floor. Low relative errors may then be achievable with this configuration.

5 CONCLUSIONS

This work attempted to conduct a fair numerical comparison of frequency domain and time-domain marine EM methods by including a realistic noise model and the frequency-dependent spectrum for source waveforms that are used in practice. The 1D resolution tests presented here may be oversimplified for three dimensional reservoirs, but nonetheless they offer some practical insights into the suggestion that time-domain methods may be superior to frequency-domain methods for marine applications.

The square wave used for the time-domain step-on response requires a fundamental frequency at least as low as 0.1 Hz in order to capture a geologic signal from a 1 km deep resistive reservoir and to reach the DC response limit. However, the rapid fall-off of the higher order harmonics makes this signal significantly weaker at the higher frequencies where the sensitivity to the reservoir is maximal. To compensate for this, the time-domain method requires a much longer stacking time to obtain the $\sqrt{N}$ noise reduction that puts the time-domain resolution on par with that obtained with a broadband frequency-domain waveform. This longer stacking time limits the utility of time-domain methods since the movement of the EM transmitter would introduce significant bias. Conversely, shorter stacking times without this bias will be limited by lower

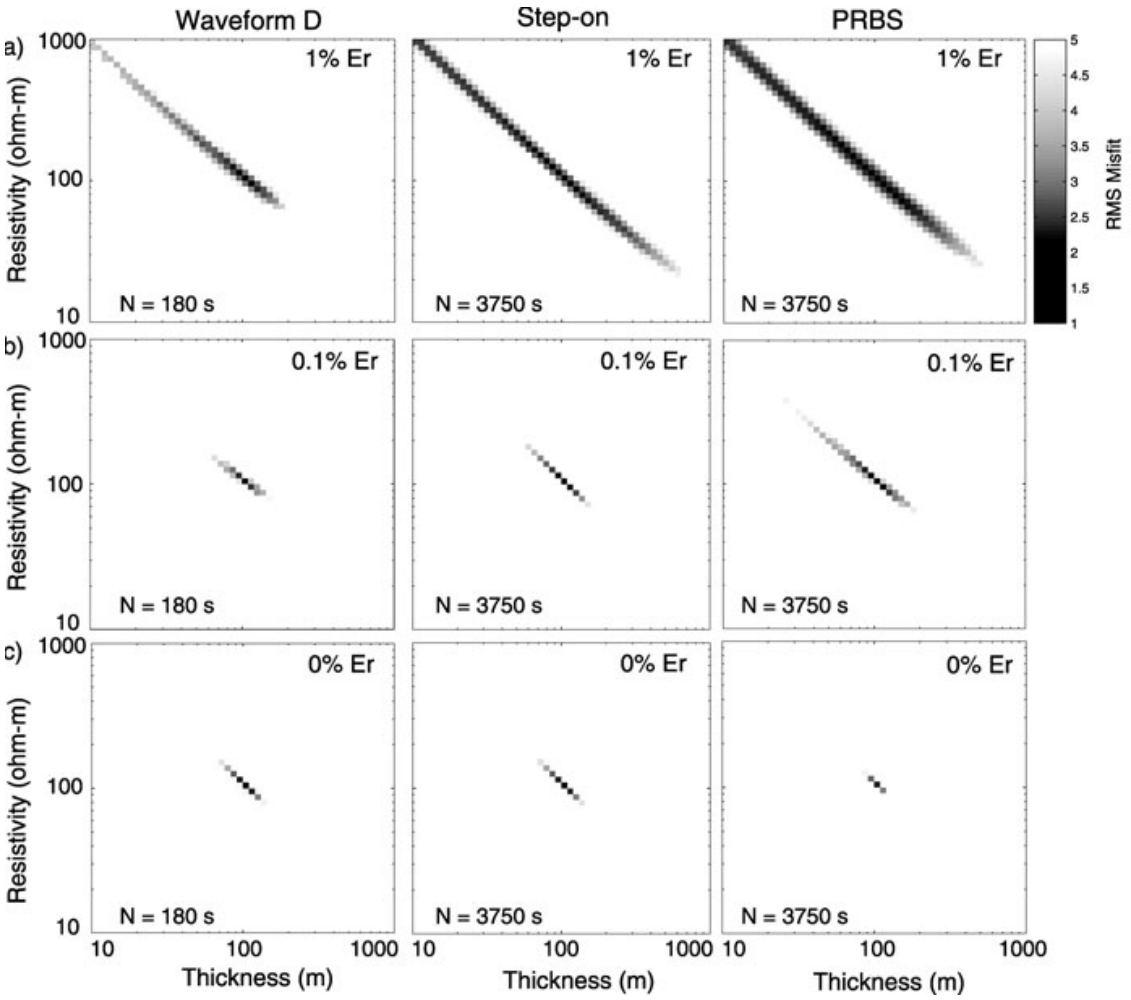

Figure 9. Misfit surfaces as a function of relative error E_r for the frequency-domain waveform D ($N = 180$ s) and time-domain step-on ($N = 3750$ s) and time-domain PRBS (order $n = 10$, $N = 3750$ s) responses. The water depth was 100 m.

signal-to-noise ratios. The alternative to this is to park the source on the seafloor for each time-domain stacking sequence, which would severely limit the amount of transmission locations for a given amount of survey time.

The pseudo-random binary sequence (PRBS) method used for the time-domain impulse responses was found to suffer from low resolution when using stacking times comparable to the frequency domain data. The PRBS is inherently a lower-power waveform since it distributes the power to both the even and odd harmonics, and therefore requires a longer stacking time to match the resolution obtainable with a broadband frequency domain waveform.

A broad sampling of the frequency spectrum is beneficial for constraining both shallow and deep structures, particularly when the host resistivity is unknown. However, since CSEM responses vary smoothly as a function of frequency, the dense sampling of frequencies inherent in the time-domain method is unnecessary. The sparse distribution of high power odd harmonics in broadband frequency domain waveforms allows for higher signal-to-noise ratios at frequencies with the largest sensitivities to the target response and hence provides better resolution for a given stacking time.

Most of the resolution results found here could have been predicted simply by careful consideration of the source power spectra shown in Fig. 3, where the differences in power explain most of the resolution differences. For perfect noise-free data or when there is unlimited time available for stacking, the PRBS offers the highest resolution. For the realistic case of noisy data and stacking time-limits imposed by the motion of the deep-towed transmitter, the broadband frequency domain waveform offers the best resolution due to its high signal-to-noise ratio.

In closing, consider the time required for a 40 km CSEM tow line, which is representative of a survey using 21 receivers spaced every kilometre with data to 10 km in-tow and out-tow range. At a tow speed of 2 kt (1 m/s), a frequency domain source using a broadband waveform and $N = 60$ s data stacks would take only 11 hours to produce 667 transmission bins spaced every 60 m along the tow-line. Since the time-domain methods discussed here require a factor of 10 or more increase in stacking time to match the resolution of the broadband frequency-domain source, a time-domain survey would require several days in order to match what could be done in the frequency domain in about half a day.

ACKNOWLEDGEMENTS

We thank Samer Naif for assistance with the SERPENT magnetotelluric data, which were collected under NSF grant OCE-0841114. Steve Constable, Rune Mittet and one anonymous reviewer provided helpful suggestions. This work was supported by the Seafloor Electromagnetic Methods Consortium at the Scripps Institution of Oceanography.

REFERENCES

Amundsen L., Løseth L., Mittet R., Ellingsrud S. and Ursin B. 2006. Decomposition of electromagnetic fields into upgoing and downgoing components. *Geophysics* **71**(5), G211–G223.

Anderson W.L. 1982. Fast Hankel-transforms using related and lagged convolutions. *ACM Transactions on Mathematical Software* **8**(4), 344–368.

Andreis D. and MacGregor. 2008. Controlled-source electromagnetic sounding in shallow water: Principles and applications. *Geophysics* **73**(1), F21–F32.

Arfken G. and Weber H. 2005. *Mathematical methods for physicists*. Elsevier.

Chave A.D. and Cox C.S. 1982. Controlled electromagnetic sources for measuring electrical-conductivity beneath the oceans. 1. Forward problem and model study. *Journal Of Geophysical Research-Solid Earth* **87**, 5327–5338.

Connell D. 2011. *A Comparison of Marine Time-Domain and Frequency-Domain Controlled Source Electromagnetic Methods*. Master's thesis, University of California San Diego.

Constable 2010. Ten years of marine CSEM for hydrocarbon exploration. *Geophysics* **75**(5), 75A67–75A81.

Constable S.C., Orange A.S., Hoversten G.M. and Morrison H.F. 1998. Marine magnetotellurics for petroleum exploration Part I: A sea-floor equipment system. *Geophysics* **63**(03), 816–825.

Constable S. and Weiss C.J. 2006. Mapping thin resistors and hydrocarbons with marine EM methods: Insights from 1D modeling. *Geophysics* **71**(2), G43–G51.

Cox C. 1980. Electromagnetic induction in the oceans and inferences on the constitution of the earth. *Geophysical Surveys* **4**, 137–156.

Duncan P.M., Hwang A., Edwards R.N., Bailey R.C. and Garland G. D. 1980. The development and applications of a wide band electromagnetic sounding system using a pseudo noise source. *Geophysics*, **45**(8), 1276.

Ellingsrud S., Eidesmo T., Johansen S., Sinha M.C., MacGregor L. M. and Constable 2002. Remote sensing of hydrocarbon layers by seabed logging (SBL): Results from a cruise offshore Angola. *The Leading Edge* **21**, 972–982.

Guptasarma D. and Singh B. 1997. New digital linear filters for Hankel J(0) and J(1) transforms. *Geophysical Prospecting* **45**(5), 745–762.

Hoversten G.M., Constable S.C. and Morrison H.F. 2000. Marine magnetotellurics for base-of-salt mapping: Gulf of Mexico field test at the Gemini structure. *Geophysics* **65**(5), 1476–1488.

Hoversten G.M., Morrison H.F. and Constable S.C. 1998. Marine magnetotellurics for petroleum exploration, Part II: Numerical analysis of subsalt resolution. *Geophysics* **63**(03), 826–840.

Key K. 2003. *Application of broadband marine magnetotelluric exploration to a 3D salt structure and a fast spreading ridge*. Ph.D. thesis, University of California, San Diego.

Key K. 2009. 1D inversion of multicomponent, multifrequency marine CSEM data: Methodology and synthetic studies for resolving thin resistive layers. *Geophysics* **74**(2), F9–F20.

Key K. 2010. Preliminary Cruise Report for SERPENT: Serpentinite, Extension and Regional Porosity Experiment across the Nicaraguan Trench, http://marineemlab.ucsd.edu/Projects/SERPENT/SERPENTCruiseReport.pdf

Key 2011. Marine electromagnetic studies of seafloor resources and tectonics. *Surveys In Geophysics*.

Key K.W., Constable S.C. and Weiss C.J. 2006. Mapping 3D salt using the 2D marine magnetotelluric method: Case study from Gemini Prospect, Gulf of Mexico. *Geophysics* **71**(1), B17–B27.

Kong F.N. 2007. Hankel transform filters for dipole antenna radiation in a conductive medium. *Geophysical Prospecting* **55**(1), 83–89.

Li Y.-G. and Constable 2010. Transient Electromagnetic in Shallow Water: Insights From 1D Modeling. *Chinese Journal Of Geophysics-Chinese Edition* **53**(3), 737–742.

MacGregor L., Andreis D., Tomlinson J. and Barker N. 2006. Controlled-source electromagnetic imaging on the Nuggets-1 reservoir. *The Leading Edge* **25**(8), 984–992.

Mittet R. 2008. Normalized amplitude ratios for frequency-domain CSEM in very shallow water. *First Break* **26**, 47–54.

Mittet R. and Schaug-Pettersen 2008. Shaping optimal transmitter waveforms for marine CSEM surveys. *Geophysics* **73**(3), F97–F104.

Myer D., Constable S. and Key K. 2011. Broad-band waveforms and robust processing for marine CSEM surveys. *Geophysical Journal International* **184**, 689–698.

Newman G., Hohmann G. and Anderson W. 1986. Transient electromagnetic response of a three-dimensional body in a layered earth. *Geophysics* **51**(8), 1608–1627.

Orange A., Key K. and Constable 2009. The feasibility of reservoir monitoring using time-lapse marine CSEM. *Geophysics* **74**(2), F21–F29.

Percival D.B. and Walden A.T. 1993. *Spectral analysis for physical applications: Multitaper and conventional univariate techniques*. Cambridge University Press, Cambridge.

Um E.S. and Alumbaugh D.L. 2007. On the physics of the marine controlled-source electromagnetic method. *Geophysics* **72**(2), WA13–WA26.

Weiss C. 2007. The fallacy of the "shallow-water problem" in marine CSEM exploration. *Geophysics* **72**(6), A93–A97.

Young P.D. and Cox C.S. 1981. Electromagnetic active source sounding near the East Pacific Rise. *Geophysical Research Letters* **8**, 1043–1046.

Ziolkowski A., Hobbs B.A. and Wright D. 2007. Multitransient electromagnetic demonstration survey in France. *Geophysics* **72**(4), F197–F209.

Ziolkowski A., Parr R., Wright D., Nockles V., Limond C., Morris E. and Linfoot 2010. Multi-transient electromagnetic repeatability experiment over the North Sea Harding field. *Geophysical Prospecting* **58**(6), 1159–1176.

APPENDIX A: CALCULATING TIME-DOMAIN RESPONSES FROM FREQUENCY DOMAIN RESPONSES

The time-domain response $g(t)$ for an arbitrary source function $s(t)$ at time t is described by the convolution

$$g(t) = \int_0^t f(t')s(t-t')dt' \qquad t \geq 0, \tag{A1}$$

where $f(t)$ is the impulse response of the model. From the convolution theorem, the frequency domain equivalent of equation (A1) is

$$\hat{g}(\omega) = \hat{f}(\omega)\hat{s}(\omega), \tag{A2}$$

where the Fourier transform pairs are

$$\hat{g}(\omega) = \int_{-\infty}^{\infty} g(t)e^{-i\omega t}\,dt, \tag{A3}$$

$$g(t) = \frac{1}{2\pi}\int_{-\infty}^{\infty} \hat{g}(\omega)e^{i\omega t}\,d\omega. \tag{A4}$$

Since $g(t) = 0$ for $t < 0$ due to causality, equation (A3) reduces to

$$\hat{g}(\omega) = \int_{-\infty}^{\infty} g(t)e^{-i\omega t}\,dt = \int_0^{\infty} g(t)e^{-i\omega t}\,dt = u(\omega) + iv(\omega), \tag{A5}$$

where

$$u(\omega) = \int_0^{\infty} g(t)\cos(\omega t)\,dt, \tag{A6}$$

$$v(\omega) = -\int_0^{\infty} g(t)\sin(\omega t)\,dt. \tag{A7}$$

Inserting the even function u and the odd function v into equation (A4) gives

$$g(t) = \frac{1}{2\pi}\int_{-\infty}^{\infty} [u(\omega) + iv(\omega)]\,[\cos(\omega t) + i\sin(\omega t)]\,d\omega, \tag{A8}$$

which by symmetry can be reduced to

$$g(t) = \frac{1}{\pi}\int_0^{\infty} u(\omega)\cos(\omega t)\,d\omega - \frac{1}{\pi}\int_0^{\infty} v(\omega)\sin(\omega t)\,d\omega. \tag{A9}$$

In order to satisfy $g(t) = 0$ for $t < 0$, the following relationship is required:

$$\int_0^{\infty} u(\omega)\cos(\omega t)\,d\omega = \int_0^{\infty} v(\omega)\sin(\omega t)\,d\omega, \qquad t < 0, \tag{A10}$$

where the sign of the term $\sin(\omega t)$ reverses when $t > 0$. Consequently, the time-domain response can be evaluated by using either a cosine or sine transform:

$$g(t) = \frac{2}{\pi}\int_0^{\infty} u(\omega)\cos(\omega t)\,d\omega, \tag{A11}$$

$$= -\frac{2}{\pi}\int_0^{\infty} v(\omega)\sin(\omega t)\,d\omega. \tag{A12}$$

In addition to the relationship given by equation (A10), the real and imaginary parts of $\hat{g}(\omega)$ are related by Kramers–Kronig relations, where the real part of the response can be predicted from the imaginary part and vice versa (e.g., Arfken and Weber 2005).